



An Efficient Structure Manipulation Strategy of Preparing Vanadium Carbide, V_8C_7/C , for Improving Lithium and Zinc Storage

Xuena Xu¹ · Liluo Shi¹ · Yan Xu¹ · Limei Sun¹ · Ming Song¹

Received: 28 April 2022 / Accepted: 8 August 2022 / Published online: 1 September 2022
© The Minerals, Metals & Materials Society 2022

Abstract

Vanadium carbide, V_8C_7/C , with low crystallization and loose inner structure is successfully designed via a convenient method of optimizing annealing time. This structure increases electrochemical reaction active sites, decreases lattice strain, and accelerates lithium/zinc ions transport, effectively improving the lithium and zinc storage ability of V_8C_7/C . Profiting from these advantages, V_8C_7/C with this structure exhibits outstanding electrochemical activity in lithium ion batteries and aqueous zinc ion batteries. In lithium ion batteries, V_8C_7/C with low crystallization and a loose inner structure delivers a higher capacity of $\sim 285.2 \text{ mAh g}^{-1}$ compared to the product with high crystallization and a tight inner structure ($\sim 131 \text{ mAh g}^{-1}$) after 50 cycles at 0.2 A g^{-1} . Even at a high current density of 1.0 A g^{-1} , the capacity can still be stabilized at $\sim 142.9 \text{ mAh g}^{-1}$ after 200 cycles. In aqueous zinc ion batteries, this designed structure also shows good cycling ($\sim 71.8 \text{ mAh g}^{-1}$ at 1.0 A g^{-1} after 200 cycles) and rate ($\sim 84.7 \text{ mAh g}^{-1}$ at 5.0 A g^{-1}) performance.

Keywords V_8C_7 · annealing time · lithium ion batteries · zinc ion batteries · electrochemical performance

Introduction

With the enhanced market demand for energy storage devices,^{1–3} monovalent and multivalent ion batteries have been extensively developed.^{4–7} Lithium ion batteries (LIBs), as the common monovalent ion battery, are commercialized and widely applied in various fields. However, their anode material, graphite, is undergoing a security problem due to its low voltage platform ($\sim 0.1 \text{ V vs. Li/Li}^+$).^{8, 9} Another conventional anode, $Li_4Ti_5O_{12}$, has the disadvantage of a low theoretic specific capacity ($\sim 175 \text{ mAh g}^{-1}$), although its voltage plateau is safe ($\sim 1.5 \text{ V vs. Li/Li}^+$).^{10, 11} For multivalent ion batteries, aqueous zinc ion batteries (ZIBs) with features of low cost, easy assembly, and security have attracted great attention.^{12–15} Nevertheless, the radius of Zn^{2+} ($\sim 0.74 \text{ \AA}$) is larger than that of Li^+ ($\sim 0.69 \text{ \AA}$), meaning that it is more difficult to find suitable materials for zinc storage.^{12, 16} Therefore, the suitable electrode materials with

superior lithium- and zinc-storage ability are anticipated to be developed.

Recently, vanadium-based compounds, including vanadium oxides, vanadium sulfide, and vanadium carbides, have been largely explored in LIBs and ZIBs owing to their abundant valence states and diverse structures.^{17–30} Especially, vanadium carbides, relying on good electronic conductivity and high chemical stability, are rapidly being brought into focus in energy storage devices.^{31–38} Gogotsi et al. reported V_2CT_x as a promising anode in LIBs, and V_2CT_x shows an unobvious voltage platform and a high specific capacity.³⁷ Yang et al. researched the electrochemical performance of V_2CT_x as the anode in sodium-ion batteries and discussed its charge storage process.³⁸ Nevertheless, the use of hydrofluoric acid in synthesizing V_2CT_x will cause a huge danger and impede its mass production.^{34–38} Therefore, another kind of vanadium carbide, V_8C_7 , which can be facilely and safely produced, has captured attention.^{31, 39} Simultaneously, V_8C_7 possesses a higher stability and electronic conductivity in contrast to V_2CT_x .³² These advantages suggest the great potential of V_8C_7 for lithium and zinc storage. However, it has rarely been reported.

In this work, vanadium carbide, V_8C_7/C , was synthesized and employed as the anode in LIBs and the cathode in ZIBs. To stimulate the lithium- and zinc-storage activity

✉ Ming Song
mings@xzit.edu.cn

¹ School of Materials and Chemical Engineering,
Xuzhou University of Technology, Xuzhou 221018,
People's Republic of China

of V_8C_7/C , a method of adjusting the annealing time was adopted. Different from designing complex structures for active materials,^{40–44} it is simple, convenient, and suitable for practical application. Through optimizing the annealing time, the crystallization and morphology of V_8C_7/C are largely modified, and the low crystallization and a loose inner structure are produced, which increases the reaction active sites and fastens the migrations of lithium/zinc ions and electron. Benefiting from this, V_8C_7/C exhibits good cycling and rate performance in LIBs and ZIBs, suggesting its high lithium- and zinc-storage abilities.

Experimental

Materials Synthesis

V_8C_7/C was synthesized through a simple solvent evaporation method, followed by post-annealing. Then, 0.234 g of NH_4VO_3 , 0.495 g of ethylene glycol, and 0.383 g of citric acid were mixed in 20 ml of distilled H_2O and stirred for 3 h. Subsequently, the solution was continuously stirred to dry at 120°C in an oil bath. The obtained powder was annealed in an Ar atmosphere at high temperature to produce V_8C_7/C . By adjusting the annealing time, a series of products were obtained: ST- V_8C_7/C (350°C for 3 h and 750°C for 5 h), MT- V_8C_7/C (350°C for 6 h and 750°C for 5 h), and LT- V_8C_7/C (350°C for 3 h and 750°C for 10 h).

Structure Characterization

Crystal structures of products were tested on an x-ray diffractometer (XRD; Ultima IV; Rigaku, Japan), with $Cu K\alpha$ line as the radiation ($\lambda = 1.5406 \text{ \AA}$). Raman spectra were obtained from a MicroRaman spectrometer (DXR-2; ThermoFisher, USA) using a laser with 632-nm excitation. The morphology of the products was observed by a scanning electron microscope (SEM; SUPRATM 55; Zeiss, Germany) and a transmission electron microscope (TEM; JEM 1011; JEOL, Japan). Energy dispersive x-ray spectroscopy (EDS) was measured using an energy dispersive x-ray spectrometer (INCAx; Oxford Instruments, UK). The lattice fringes were received from a high-resolution transmission electron microscope (HRTEM; JEM 2100F; JEOL).

Electrochemical Measurements

For the LIBs, the working electrodes were prepared using 80 wt% of V_8C_7/C -based products, 10 wt% of acetylene black, and 10 wt% of poly(vinylidene fluoride). To obtain a uniform slurry, some N-methyl-2-pyrrolidone was dropped into the mixture and hand-milled for 30 min. The slurry was then uniformly coated on a Cu foil, and dried for about 24 h in

a vacuum oven. The foil with the active material was roll-pressed and then cut into discs. The diameter of each disc was 12 mm and the mass of active material on the disc was 1.5–2.0 $mg\ cm^{-2}$. Next, the discs were assembled with lithium plates employing CR2032 coin cells. The separator was a Celgard 2400 membrane and the electrolyte was 1 M $LiPF_6$ dissolved in ethylene carbonate–dimethyl carbonate–ethyl methyl carbonate (1:1:1 in volume ratio). All the assembly operations were carried in a glove box (Super 1220/750/900; Mikrouna) filled with Ar. Electrochemical performance was tested on a battery cycler (CT300A; Neware, China). Cyclic voltammograms (CV) curves and electrochemical impedance spectra (EIS) were measured on an electrochemical workstation (CHI 660E; China).

For the ZIBs, the working electrode contained active material, acetylene black, and polytetra-fluoroethylene with a mass ratio of 7:2:1. The powders were mixed by adding some isopropanol. After drying, the film was punched into discs (diameter: 10 mm, loading mass: $\sim 2\ mg\ cm^{-2}$). A three-electrode device was used to test the electrochemical performance with a zinc plate as the counter electrode, platinum as the reference electrode, and the aqueous solution containing 2 M $ZnSO_4$ as the electrolyte.

Results and Discussion

The XRD patterns of the products at different annealing times were measured to study their influence on the crystalline nature. In the XRD pattern of the precursor (see supplementary figure S1), no obvious diffraction peaks appear, suggesting no crystalline compound generating. After annealing at different times, the XRD patterns of the obtained products in Fig. 1a show the clear diffraction peaks, ascribed to the V_8C_7 phase (JCPDS Card, No. 35–0786). The space group is $P4_132$ and the lattice parameters are $a = b = c = 8.334 \text{ \AA}$ and $\alpha = \beta = \gamma = 90^\circ$. The corresponding diffraction peaks of the products are stronger with the increase of annealing time, which indicates that a long annealing time is responsible for high crystallization. Among the products, ST- V_8C_7/C with a lower crystallization has a low lattice strain and loose inner structure, favorable to ions and electron transport. Therefore, ST- V_8C_7/C is anticipated to achieve high electrochemical activity. To further analyze the product components, Raman spectra of the products are depicted in Fig. 1b. All the products exhibit two wide peaks near $1338\ cm^{-1}$ and $1598\ cm^{-1}$, ascribed to the D band and G band of carbon. The weak peak centered at $225\ cm^{-1}$ originates from vanadium carbide, illustrating the successful synthesis of V_8C_7/C .^{45, 46} The signals of V and C collected by EDS also confirm the existence of ST- V_8C_7/C , which is clearly observed (see supplementary figure S2).

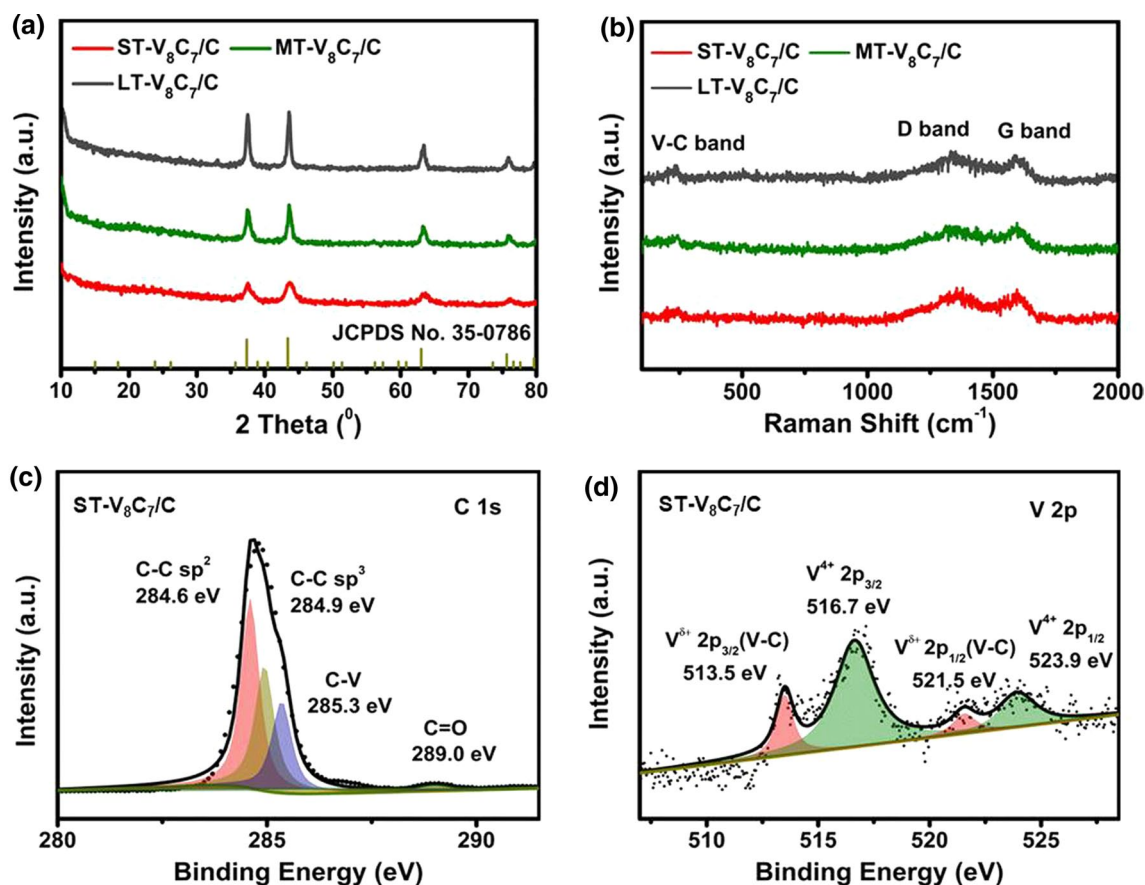


Fig. 1 (a) XRD patterns and (b) Raman spectra of ST- V_8C_7/C , MT- V_8C_7/C , and LT- V_8C_7/C . XPS spectra of ST- V_8C_7/C : (c) C 1s, (d) V 2p.

In order to identify the valence state of the products, the x-ray photoelectron spectrometry (XPS) was tested. Comparing the survey spectra of the precursor and the ST- V_8C_7/C (see supplementary figure S3), the lack of an N signal in the ST- V_8C_7/C indicates a complete decomposition of NH_4VO_3 during the annealing. Figure 1c shows a C 1s high-resolution spectrum of ST- V_8C_7/C . The peaks near 284.6 and 284.9 eV are attributed to C–C in sp^2 and C–C in sp^3 .^{47, 48} The peak around 285.3 eV belongs to the C–V bond, proving the formation of vanadium carbide.⁴⁹ In Fig. 1d, the V 2p spectrum is divided into four peaks, where $V^{\delta+} 2p_{3/2}$ and $V^{\delta+} 2p_{1/2}$ peaks are located at 513.5 and 521.5 eV standing for the V–C bond ($0 < \delta < 4$).^{31, 50} The peaks of V^{4+} at 516.7 eV and 523.9 eV arise from vanadium oxidized by the absorbed oxygen on the product surface, which is also proved by the –OH peaks and the absorbed oxygen in the O 1s spectrum (see supplementary figure S4).^{51, 52} Based on this analysis, the appearance of C 1s peaks representing the C–V bond and the mixed valence $V^{\delta+}$ peaks shows the carbonization of the oxide to form a carbide, illustrating that vanadium carbide has been successfully synthesized.⁵¹ In contrast, the C 1s and V 2p high-resolution spectra of the precursor (see supplementary figure S5a and S5b) are distinctly different

from those of the annealed products. The C 1s peaks around 284.6 eV, 285.1 eV, 286.8 eV, and 289.0 eV are attributed to the C–C in sp^2 , C–C in sp^3 , C–O/C–H, and C=O, respectively. The V 2p peaks near 517.2 eV and 524.8 eV belong to V^{5+} , and the weak peaks around 516.7 and 524.0 eV arise from V^{4+} .⁵³ There are no characteristic peaks related to vanadium carbide, according to the XPS results of the precursor, while the peaks of vanadium oxide and some organics are observed. Therefore, it is inferred that annealing the precursor at a high temperature causes the decomposition of small organic molecules, accompanied by the carbonization of vanadium oxide and the formation of vanadium carbide, V_8C_7/C . More importantly, on the premise of V_8C_7 phase formation, a shorter annealing time results in lower crystallization, which is more beneficial to electrochemical storage.

The microscopic morphology of the products is closely related to their electrochemical performance. Figure 2 reveals the influence of annealing time on the morphology of the products. As observed in Fig. 2a–c, SEM images of ST- V_8C_7/C , MT- V_8C_7/C and LT- V_8C_7/C display a similar morphology, in which numerous micron-grade bulks are presented, inherited from the morphology of the precursor (see supplementary figure S6). Next, the micron bulks

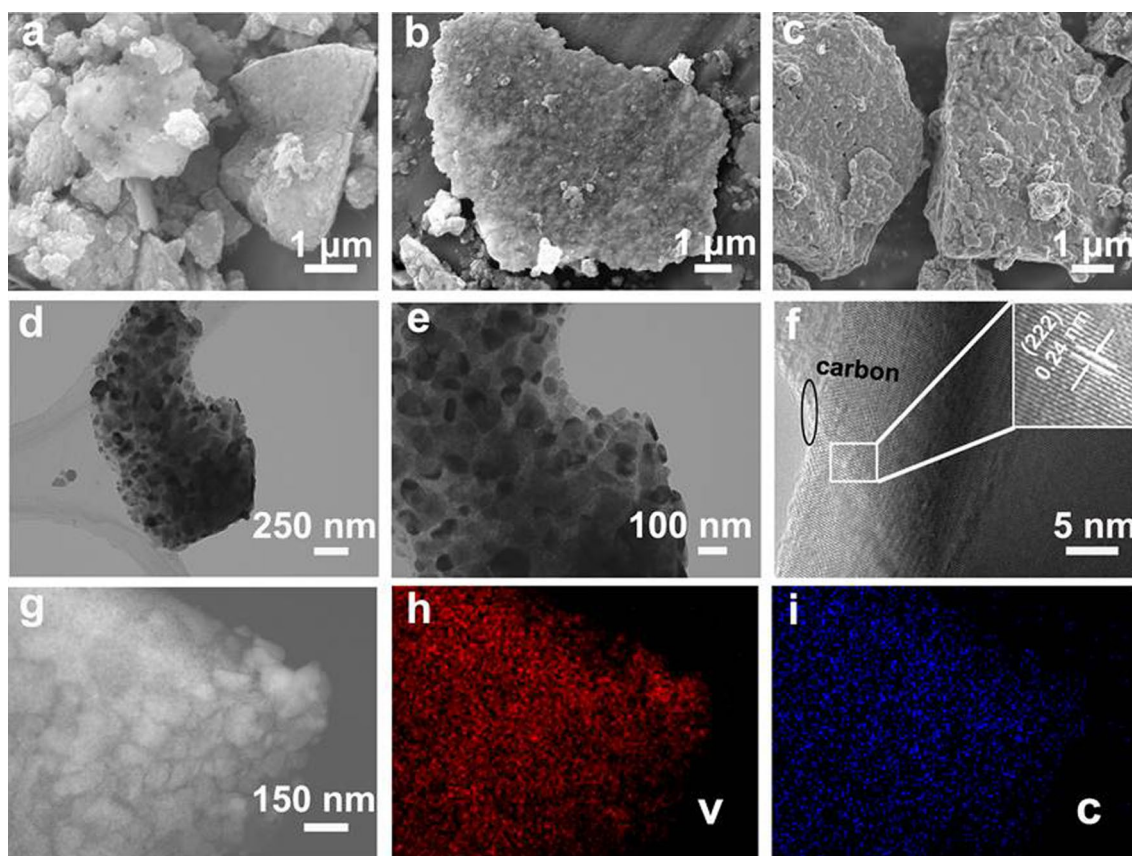


Fig. 2 SEM images of (a) ST- V_8C_7/C , (b) MT- V_8C_7/C and (c) LT- V_8C_7/C . (d, e) TEM, (f) HRTEM images, and (g–i) element maps of ST- V_8C_7/C .

are further enlarged by TEM. Figure 2d and e shows the TEM images of ST- V_8C_7/C , where the V_8C_7 nanoparticles with a size of ~ 200 nm are surrounded by carbon. Different from the close contact between the nanoparticles in MT- V_8C_7/C and LT- V_8C_7/C (see supplementary figure S7), ST- V_8C_7/C exhibits a loose inner structure and numerous voids, owing to the shorter annealing time. This special structure increases the contact area between the electrolyte and the active material, alleviates volume expansion during charging/discharging, and accelerates ion and electron diffusion. Moreover, the encircling carbon around the ST- V_8C_7 enhances electronic conductivity and prevents nanoparticle aggregation. A HRTEM image of ST- V_8C_7/C is depicted in Fig. 2f. The clear lattice fringes with the spacing of 0.24 nm are ascribed to the $\{222\}$ of V_8C_7 . An amorphous carbon layer at the edge of the product is marked by a black circle, suggesting the existence of carbon. Element maps of ST- V_8C_7/C in Fig. 2g–i illustrate the uniform distribution of elements V and C in the product.

To explore the lithium-storage ability of V_8C_7/C -based products, the electrochemical performance in the LIBs was tested. First of all, voltage windows were optimized to obtain a good electrochemical performance (see

supplementary figure S8), and 0.02–3 V was chosen for testing according to the cycling performance under different voltage ranges. Figure 3a displays the first discharge/charge curves of ST- V_8C_7/C , MT- V_8C_7/C and LT- V_8C_7/C at 0.2 A g^{-1} . The analogous curve shapes of the three products with a non-obvious voltage platform reveal their similar lithium-storage behaviors. On further observation, ST- V_8C_7/C delivers a reversible capacity of $\sim 222.5 \text{ mAh g}^{-1}$, higher than those of MT- V_8C_7/C ($\sim 170.5 \text{ mAh g}^{-1}$) and LT- V_8C_7/C ($\sim 114.5 \text{ mAh g}^{-1}$). This suggests a higher lithium storage activity of ST- V_8C_7/C , profiting from its loose inner structure and the increased lithium-storage sites. The capacity loss in the first cycle is probably due to the formation of solid-electrolyte-interphase (SEI) film, Li-ion irreversible insertion into defects, and electrolyte decomposition.^{34, 54} In subsequent cycles, the overlapping discharge/charge curves indicate good electrochemical reversibility (see supplementary figure S9). Such an electrochemical behavior of V_8C_7/C -based products is similar to that of V_2CT_x in LIBs.³⁷ CV curves of ST- V_8C_7/C at various scan rates (see supplementary figure S10) exhibit non-obvious redox peaks, consistent with the discharge/charge curves.³⁸ These may be due to the low crystalline

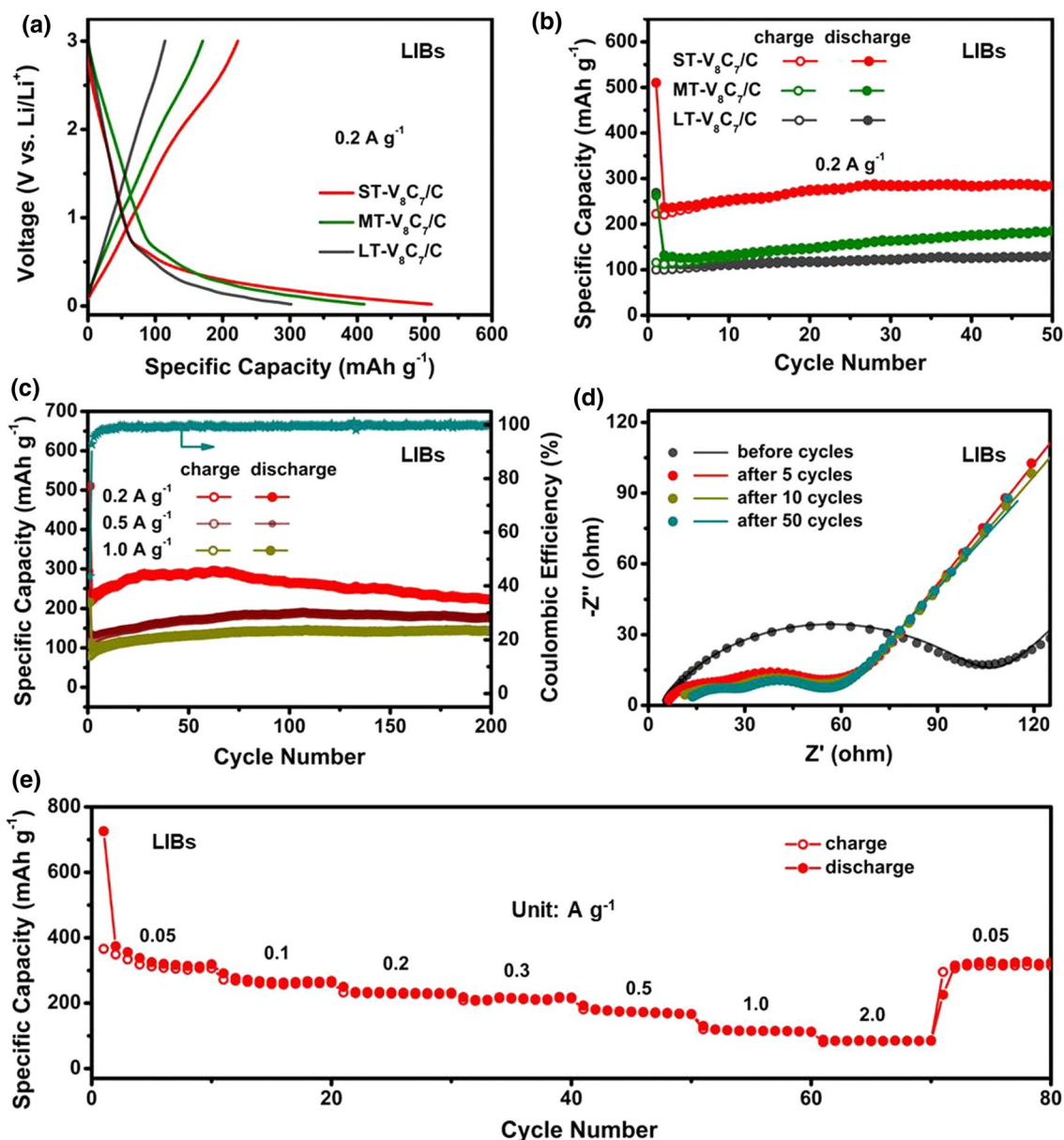
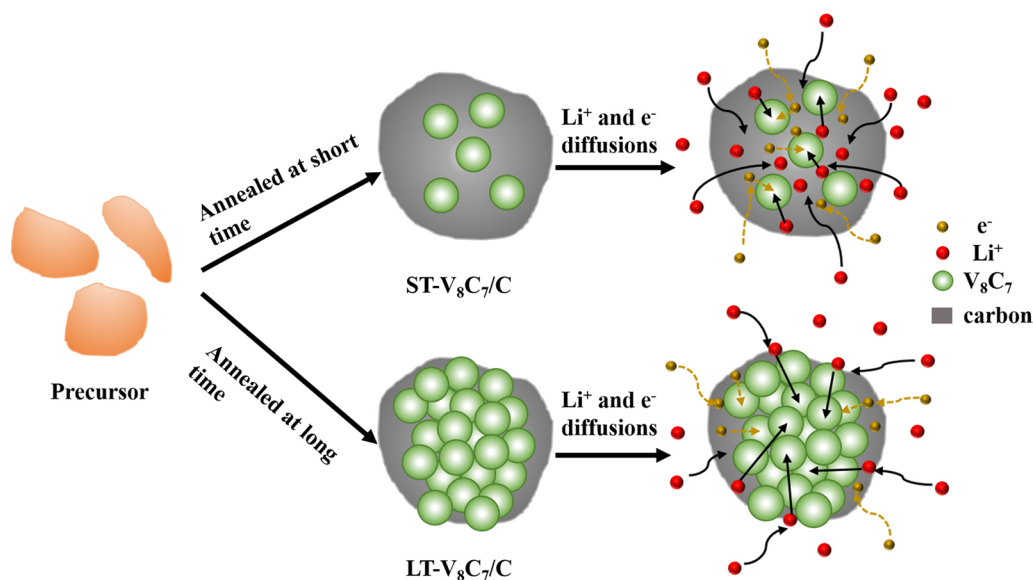


Fig. 3 Electrochemical performances of V_8C_7/C -based products in LIBs: (a) the first discharge/charge curves and (b) the compared cycling performance of ST- V_8C_7/C , MT- V_8C_7/C and LT- V_8C_7/C at 0.2 A g^{-1} . (c) Cycling performance of ST- V_8C_7/C at 0.2 A g^{-1} , 0.5 A g^{-1}

g^{-1} , and 1.0 A g^{-1} . (d) Nyquist plots of ST- V_8C_7/C after different cycle numbers. (e) Rate performance of ST- V_8C_7/C at various current densities.

of ST- V_8C_7/C . Figure 3b shows the compared cycling performance of ST- V_8C_7/C , MT- V_8C_7/C and LT- V_8C_7/C at 0.2 A g^{-1} . After 50 cycles, ST- V_8C_7/C , MT- V_8C_7/C and LT- V_8C_7/C retain discharge capacities of 285.2 mAh g^{-1} , 186 mAh g^{-1} , and 131 mAh g^{-1} , respectively. The high capacity of ST- V_8C_7/C in the cycling process suggests its higher electrochemical activity. Based on the results, ST- V_8C_7/C shows the higher lithium-storage ability in contrast to MT- V_8C_7/C and LT- V_8C_7/C , which is related to the low crystallization, loose inner space, and more active sites.

The cycling performance of ST- V_8C_7/C at different current densities was also tested. As shown in Fig. 3c, ST- V_8C_7/C maintains a discharge capacity of 223.1 , 177.3 , or 142.9 mAh g^{-1} at 0.2 A g^{-1} , 0.5 A g^{-1} , or 1.0 A g^{-1} after 200 cycles, respectively. This reveals a good electrochemical stability of ST- V_8C_7/C even at high current densities. The capacity increase before 20 cycles at 0.2 A g^{-1} is because of electrode activation and the expansion of the lithium-storage space in the electrode material, while the capacity decrease after 50 cycles is ascribed to structural damage



Scheme 1 Schematic of lithium ion and electron diffusion in ST- V_8C_7/C and LT- V_8C_7/C .

of the electrode material, electrode polarization, and the side reactions.^{55, 56} As observed, the coulombic efficiency in the first cycle is 43.6%. The low coulombic efficiency is due to the irreversible lithium ion consumption originating from the SEI film, lattice defects, and side reactions, such as electrolyte decomposition. To explore the reasons for the outstanding cycling performance of ST- V_8C_7/C , the EIS spectra were measured after different cycle numbers. In Fig. 3d, Nyquist plots before cycles have one semicircle in high to medium frequencies, related to charge transfer resistance (R_{ct}), with a slope in low frequencies representing lithium ion diffusion in the electrode material. In contrast, two semicircles in high to medium frequencies are observed in the Nyquist plots after cycles, indicating the existence of SEI film resistance (R_f) because of the formation of SEI film. After fitting by equivalent circuits (see supplementary figure S11), the Nyquist plots before and after cycles exhibit distinctly different R_{ct} and R_f values. As revealed in Table S1, the R_{ct} value drops to 45.3 Ω from 99.7 Ω in 5 cycles, and tends to be stable in subsequent cycles, which implies a stable charge transfer behavior during cycling. The R_f value is 10.4 Ω after 5 cycles and 15.1 Ω after 50 cycles, suggesting a steady SEI film interface. Such a stable charge transfer and SEI film interface are responsible for the excellent electrochemical performance of ST- V_8C_7/C . Figure 3e shows the rate performance of ST- V_8C_7/C , where specific capacities of 325.1 mAh g^{-1} at 0.05 A g^{-1} , 264.4 mAh g^{-1} at 0.1 A g^{-1} , 232.4 mAh g^{-1} at 0.2 A g^{-1} , 216.1 mAh g^{-1} at 0.3 A g^{-1} , 174 mAh g^{-1} at 0.5 A g^{-1} , 115.3 mAh g^{-1} at 1.0 A g^{-1} , and 85.6 mAh g^{-1} at 2.0 A g^{-1} are observed. A high capacity at high current densities indicates the rapid reaction kinetics of ST- V_8C_7/C . The adjacent discharge/charge

curves of ST- V_8C_7/C at various current densities reveal the small voltage polarization (see supplementary figure S12). These results illustrate that ST- V_8C_7/C has rapid lithium ion and electron diffusion, which can be attributed to its low crystalline nature, loose inner space, and more active sites.

To clearly explain the cause of the improved lithium-storage ability of ST- V_8C_7/C , a schematic of lithium ion and electron diffusion in the products is described in Scheme 1. ST- V_8C_7/C annealed in a short time has a looser inner structure and more space between the nanoparticles in comparison with LT- V_8C_7/C . Therefore, the electrolyte in ST- V_8C_7/C more easily permeates the inner nanoparticles of the electrode, and the transport paths of the lithium ions and electrons are shorter. This means that the interior nanoparticles can also be fully utilized, greatly increasing electrochemical active sites and improving the specific capacity of ST- V_8C_7/C . In contrast, the tight inner structure of LT- V_8C_7/C makes the lithium ion and electron diffusion sluggish, which leads to difficulties for the interior nanoparticles to participate in the electrochemical reaction. Thus, by optimizing the annealing time, the ST- V_8C_7/C achieves a higher lithium-storage activity and develops a great possibility as the electrode material in LIBs.

In addition, the electrochemical performance of ST- V_8C_7/C in ZIBs was measured to investigate its zinc-storage ability. Figure 4a shows charge/discharge curves of ST- V_8C_7/C at 0.1 A g^{-1} between 0.3 V and 1.4 V. It exhibits stable voltage plateaux at 0.73 V and 0.98 V in the charge process and 0.95 V and 0.67 V in the discharge process. Similar curve shapes indicate the stable electrochemical behavior of ST- V_8C_7/C . In the first cycle, the charge/discharge capacity of ST- V_8C_7/C is 176/216.1 mAh g^{-1} . As exhibited in Fig. 4b, ST- V_8C_7/C

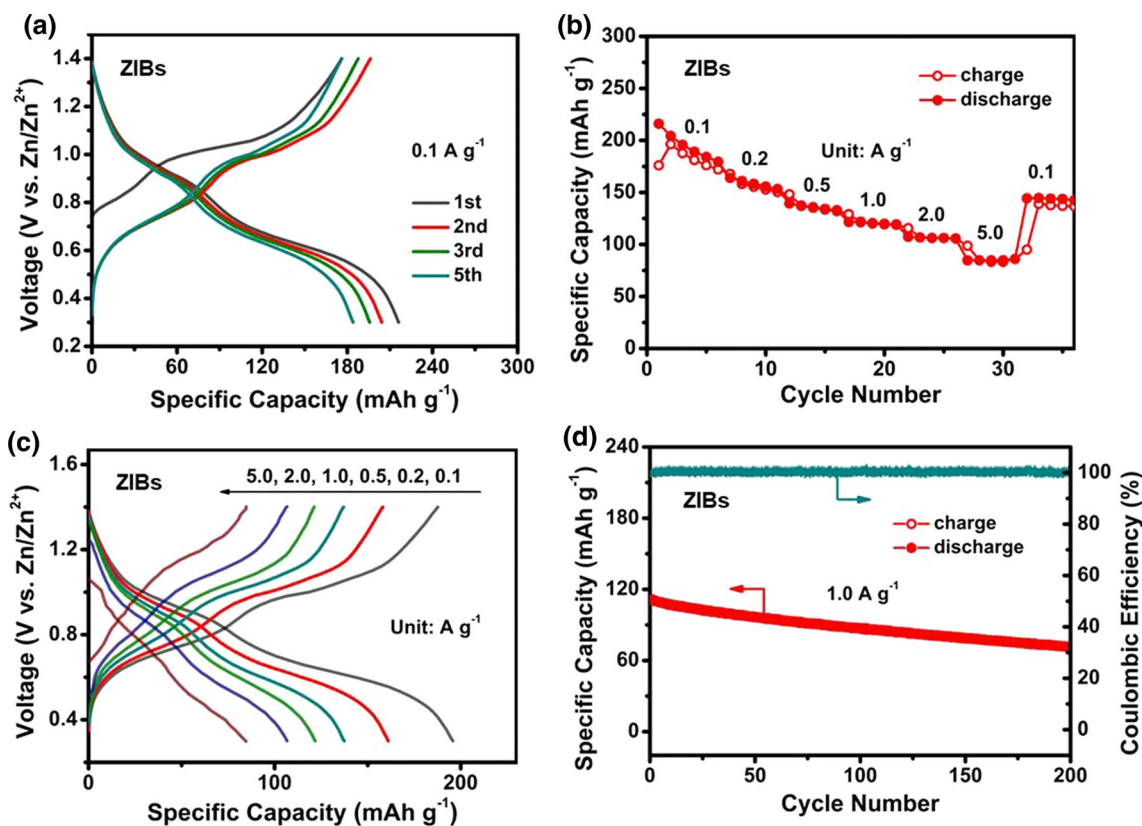


Fig. 4 Electrochemical performance of ST- V_8C_7/C in ZIBs: (a) charge/discharge curves of ST- V_8C_7/C at 0.1 A g^{-1} between 0.3 and 1.4 V, (b) rate performance, and (c) charge/discharge curves of ST-

V_8C_7/C at different current densities, (d) cycling performance of ST- V_8C_7/C at 1.0 A g^{-1} .

delivers a capacity of 195.8 mAh g^{-1} at 0.1 A g^{-1} , 161 mAh g^{-1} at 0.2 A g^{-1} , 137.4 mAh g^{-1} at 0.5 A g^{-1} , 121.8 mAh g^{-1} at 1.0 A g^{-1} , 106.7 mAh g^{-1} at 2.0 A g^{-1} , and 84.7 mAh g^{-1} at 5.0 A g^{-1} . Such rate performances suggest a fast reaction rate of ST- V_8C_7/C with zinc ions, even if at high current densities. The close charge/discharge curves of ST- V_8C_7/C in Fig. 4c also verify this point. Figure 4d depicts the cycling performance of ST- V_8C_7/C at a high current density of 1.0 A g^{-1} . After 200 cycles, ST- V_8C_7/C retains a stable capacity of 71.8 mAh g^{-1} . The corresponding coulombic efficiency is close to 100%, suggesting a reversible zinc insertion/desertion behavior in ST- V_8C_7/C . Therefore, the ST- V_8C_7/C , with low crystallization and non-compact inner structure by optimizing annealing time, not only improves electrochemical lithium storage activity in LIBs but also supports the fast zinc-storage in ZIBs.

Conclusions

Vanadium carbide, V_8C_7/C , was successfully prepared and applied in LIBs and ZIBs. Through shortening the annealing time, the V_8C_7/C with low crystallization and a loose

inner structure exhibits a higher lithium- and zinc-storage ability. This special structure increases the reaction active sites, accelerates lithium/zinc ion and electron migration, and thus raises the electrochemical activity of V_8C_7/C . In LIBs, it delivers a discharge capacity of 285.2 mAh g^{-1} at 0.2 A g^{-1} after 50 cycles. Even with the current density increased to 1.0 A g^{-1} , the capacity can be stabilized at 142.9 mAh g^{-1} after 200 cycles. Simultaneously, this product also shows a good rate and cycling performance in ZIBs. At a rate of 5.0 A g^{-1} , the high capacity of 84.7 mAh g^{-1} can be obtained. After 200 cycles at 1.0 A g^{-1} , it keeps a capacity of 71.8 mAh g^{-1} . These results indicate the designed V_8C_7/C with low crystallization and loose inner structure is suitable not only for lithium ion migration but also for the transport of zinc ions with larger radii. Meanwhile, this strategy is cost-effective and convenient in practical production. Therefore, V_8C_7/C with low crystallization and noncompact inner structure shows great potential as lithium- and zinc-storage electrode material.

Supplementary Information The online version contains supplementary material available at <https://doi.org/10.1007/s11664-022-09877-0>.

Acknowledgments M. Song thanks the financial support from National Natural Science Foundation of China [No. 22075115], Natural Science Foundation of Jiangsu Higher Education Institutions of China [19KJA430020], Jiangsu Qing Lan Project [2020], and Xuzhou Science and Technology plan Project [KC21023]. X. Xu appreciates the support from Doctor of Innovation and Entrepreneurship Project in Jiangsu Province [JSSCBS20211289], and Science and Technology Training Project in Xuzhou University of Technology [No. XKY2021201]. L. Sun is thankful for the Natural Science Foundation of Jiangsu Higher Education Institutions of China (No. 21KJA150005), and the Xuzhou “Dual initiative” Project (2020).

Conflict of interest The authors declare that they have no conflict of interest.

References

1. Y. Huang, M. Zhu, Y. Huang, Z. Pei, H. Li, Z. Wang, Q. Xue, and C. Zhi, Multifunctional Energy Storage and Conversion Devices. *Adv. Mater.* 28, 8344 (2016).
2. Y. Liu, X. Lu, F. Lai, T. Liu, P.R. Shearing, I.P. Parkin, G. He, and D.J.L. Brett, Rechargeable Aqueous Zn-Based Energy Storage Devices. *Joule* 5, 2845 (2021).
3. L. Meng, G. Wang, K.W. See, Y. Wang, Y. Zhang, C. Zang, R. Zhou, and B. Xie, Large-Scale Li-Ion Battery Research and Application in Mining Industry. *Energies* 15, 3884 (2022).
4. X. Shan, Y. Zhong, L. Zhang, Y. Zhang, X. Xia, X. Wang, and J. Tu, A Brief Review on Solid Electrolyte Interphase Composition Characterization Technology for Lithium Metal Batteries: Challenges and Perspectives. *J. Phys. Chem. C* 125, 19060 (2021).
5. Y. Zhang, S. Liu, Y. Ji, J. Ma, and H. Yu, Emerging Nonaqueous Aluminum-Ion Batteries: Challenges, Status, and Perspectives. *Adv. Mater.* 30, 1706310 (2018).
6. C. Wang, Y. Li, F. Cao, Y. Zhang, X. Xia, and L. Zhang, Employing Ni-Embedded Porous Graphitic Carbon Fibers for High-Efficiency Lithium-Sulfur Batteries. *ACS Appl. Mater. Interfaces* 14, 10457 (2022).
7. D. Zhang, J. Lu, C. Pei, and S. Ni, Electrochemical Activation, Sintering, and Reconstruction in Energy-Storage Technologies: Origin, Development, and Prospects. *Adv. Energy Mater.* 12, 2103689 (2022).
8. N.S. Choi, Z. Chen, S.A. Freunberger, X. Ji, Y.K. Sun, K. Amine, G. Yushin, L.F. Nazar, J. Cho, and P.G. Bruce, Challenges Facing Lithium Batteries and Electrical Double-Layer Capacitors. *Angew. Chem. Int. Ed.* 51, 9994 (2012).
9. C. Li, C. Zheng, F. Cao, Y. Zhang, and X. Xia, The Development Trend of Graphene Derivatives. *J. Electron. Mater.* 51, 4107 (2022).
10. L. Yu, H.B. Wu, and X.W. Lou, Mesoporous $\text{Li}_4\text{Ti}_5\text{O}_{12}$ Hollow Spheres with Enhanced Lithium Storage Capability. *Adv. Mater.* 25, 2296 (2013).
11. Y. Xiang, P. Zhao, Z. Jin, B. Chen, H. Ming, H. Zhang, W. Zhang, G. Cao, and X. Zhu, Three-Dimensional and Mesopore-Oriented Graphene Conductive Framework Anchored with Nano- $\text{Li}_4\text{Ti}_5\text{O}_{12}$ Particles as an Ultrahigh Rate Anode for Lithium-Ion Batteries. *ACS Appl. Mater. Interfaces* 10, 42258 (2018).
12. G. Fang, J. Zhou, A. Pan, and S. Liang, Recent Advances in Aqueous Zinc-Ion Batteries. *ACS Energy Lett.* 3, 2480 (2018).
13. M. Song, H. Tan, D. Chao, and H. Fan, Recent Advances in Zn-ion Batteries. *Adv. Funct. Mater.* 28, 1802564 (2018).
14. A. Konarov, N. Voronina, J.H. Jo, Z. Bakenov, Y.K. Sun, and S.T. Myung, Present and Future Perspective on Electrode Materials for Rechargeable Zinc-Ion Batteries. *ACS Energy Lett.* 3, 2620 (2018).
15. P. Yu, Y. Zeng, H. Zhang, M. Yu, Y. Tong, and X. Lu, Flexible Zn-Ion Batteries: Recent Progresses and Challenges. *Small* 15, 1804760 (2019).
16. P. He, M. Yan, G. Zhang, R. Sun, L. Chen, Q. An, and L. Mai, Layered VS_2 Nanosheet-Based Aqueous Zn Ion Battery Cathode. *Adv. Energy Mater.* 7, 1601920 (2017).
17. L. Chen, X. Gu, X. Jiang, N. Wang, J. Yue, H. Xu, J. Yang, and Y. Qian, Hierarchical Vanadium Pentoxide Microflowers with Excellent Long-Term Cyclability at High Rates for Lithium Ion Batteries. *J. Power Sources* 272, 991 (2014).
18. D. Chao, X. Xia, J. Liu, Z. Fan, C.F. Ng, J. Lin, H. Zhang, Z.X. Shen, and H.J. Fan, A V_2O_5 /Conductive-Polymer Core/Shell Nanobelt Array on Three-Dimensional Graphite Foam: A High-Rate, Ultrastable, and Freestanding Cathode for Lithium-Ion Batteries. *Adv. Mater.* 26, 5794 (2014).
19. H. Wang, X. Bi, Y. Bai, C. Wu, S. Gu, S. Chen, F. Wu, K. Amine, and J. Lu, Open-Structured $\text{V}_2\text{O}_5 \cdot n\text{H}_2\text{O}$ Nanoflakes as Highly Reversible Cathode Material for Monovalent and Multivalent Intercalation Batteries. *Adv. Energy Mater.* 7, 1602720 (2017).
20. Z. Wu, W. Qiu, Y. Chen, Y. Luo, Y. Huang, Q. Lei, S. Guo, P. Liu, M. Balogun, and Y. Tong, Etched Current Collector-Guided Creation of Wrinkles in Steel-Mesh-Supported V_6O_{13} Cathode for Lithium-Ion Batteries. *J. Mater. Chem. A* 5, 756 (2017).
21. L. Mai, Q. Wei, Q. An, X. Tian, Y. Zhao, X. Xu, L. Xu, L. Chang, and Q. Zhang, Nanoscroll Buffered Hybrid Nanostructural $\text{VO}_2(\text{B})$ Cathodes for High-Rate and Long-Life Lithium Storage. *Adv. Mater.* 25, 2969 (2013).
22. W. Cheng, G. Zeng, and M. Niederberger, Design of Vanadium Oxide Core-Shell Nanoplatelets for Lithium Ion Storage. *J. Mater. Chem. A* 3, 2861 (2015).
23. M. Yan, P. He, Y. Chen, S. Wang, Q. Wei, K. Zhao, X. Xu, Q. An, Y. Shuang, Y. Shao, K.T. Mueller, L. Mai, J. Liu, and J. Yang, Water-Lubricated Intercalation in $\text{V}_2\text{O}_5 \cdot n\text{H}_2\text{O}$ for High-Capacity and High-Rate Aqueous Rechargeable Zinc Batteries. *Adv. Mater.* 30, 1703725 (2018).
24. Y. Yang, Y. Tang, G. Fang, L. Shan, J. Guo, W. Zhang, C. Wang, L. Wang, J. Zhou, and S. Liang, Li^+ Intercalated $\text{V}_2\text{O}_5 \cdot n\text{H}_2\text{O}$ with Enlarged Layer Spacing and Fast Ion Diffusion as an Aqueous Zinc-Ion Battery Cathode. *Energy Environ. Sci.* 11, 3157 (2018).
25. P. Hu, M. Yan, T. Zhu, X. Wang, X. Wei, J. Li, L. Zhou, Z. Li, L. Chen, and L. Mai, $\text{Zn}/\text{V}_2\text{O}_5$ Aqueous Hybrid-Ion Battery with High Voltage Platform and Long Cycle Life. *ACS Appl. Mater. Interfaces* 9, 42717 (2017).
26. J. Ding, Z. Du, L. Gu, B. Li, L. Wang, S. Wang, Y. Gong, and S. Yang, Ultrafast Zn^{2+} Intercalation and Deintercalation in Vanadium Dioxide. *Adv. Mater.* 30, 1800762 (2018).
27. T. Wei, Q. Li, G. Yang, and C. Wang, An Electrochemically Induced Bilayered Structure Facilitates Long-Life Zinc Storage of Vanadium Dioxide. *J. Mater. Chem. A* 6, 8006 (2018).
28. T. Wei, Q. Li, G. Yang, and C. Wang, Highly Reversible and Long-Life Cycling Aqueous Zinc-Ion Battery Based on Ultrathin $(\text{NH}_4)_2\text{V}_{10}\text{O}_{25} \cdot 8\text{H}_2\text{O}$ Nanobelts. *J. Mater. Chem. A* 6, 20402 (2018).
29. G. Yang, T. Wei, and C. Wang, Self-Healing Lamellar Structure Boosts Highly Stable Zinc-Storage Property of Bilayered Vanadium Oxides. *ACS Appl. Mater. Interfaces* 10, 35079 (2018).
30. W. Kaveevivitchai, and A. Manthiram, High-Capacity Zinc-Ion Storage in an Open-Tunnel Oxide for Aqueous and Nonaqueous Zn-Ion Batteries. *J. Mater. Chem. A* 4, 18737 (2016).
31. Z. Zhao, Y. Liu, H. Cao, S. Gao, and M. Tu, Synthesis of Vanadium Carbide Nanopowders by Thermal Processing and Their Characterization. *Powder Technol.* 181, 31 (2008).
32. X. Chong, Y. Jiang, R. Zhou, and J. Feng, Electronic Structures Mechanical and Thermal Properties of V-C Binary Compounds. *RSC Adv.* 4, 44959 (2014).

33. Y.D. Wu, G.H. Zhang, and K.C. Chou, A Novel Method to Synthesize Submicrometer Vanadium Carbide by Temperature Programmed Reaction from Vanadium Pentoxide and Phenolic Resin. *Int. J. Refract. Met. H.* 62, 64 (2017).
34. A. VahidMohammadi, A. Hadjikhani, S. Shahbazmohamadi, and M. Beidaghi, Two-Dimensional Vanadium Carbide (MXene) as a High-Capacity Cathode Material for Rechargeable Aluminum Batteries. *ACS Nano* 11, 11135 (2017).
35. X. Zhang, Z. Zhang, and Z. Zhou, MXene-Based Materials for Electrochemical Energy Storage. *J. Energy Chem.* 27, 73 (2018).
36. Y. Dall'Agnese, P.L. Taberna, Y. Gogotsi, and P. Simon, Two-Dimensional Vanadium Carbide (MXene) as Positive Electrode for Sodium-Ion Capacitors. *J Phys Chem Lett.* 6, 2305 (2015).
37. M. Naguib, J. Halim, J. Lu, K.M. Cook, L. Hultman, Y. Gogotsi, and M.W. Barsoum, New Two-Dimensional Niobium and Vanadium Carbides as Promising Materials for Li-ion Batteries. *J. Am. Chem. Soc.* 135, 15966 (2013).
38. S.M. Bak, R. Qiao, W. Yang, S. Lee, X. Yu, B. Anasori, H. Lee, Y. Gogotsi, and X.Q. Yang, Na-ion Intercalation and Charge Storage Mechanism in 2D Vanadium Carbide. *Adv. Energy Mater.* 7, 1700959 (2017).
39. X. Chong, Y. Jiang, R. Zhou, and J. Feng, The Effects of Ordered Carbon Vacancies on Stability and Thermomechanical Properties of V_8C_7 Compared with VC. *Sci. Rep.* 6, 34007 (2016).
40. S. Ni, J. Liu, D. Chao, and L. Mai, Vanadate-Based Materials for Li-ion Batteries: the Search for Anodes for Practical Applications. *Adv. Energy Mater.* 9, 1803324 (2019).
41. R. Li, F. Xing, T. Li, H. Zhang, J. Yan, Q. Zheng, and X. Li, Intercalated Polyaniline in V_2O_5 as a Unique Vanadium Oxide Bronze Cathode for Highly Stable Aqueous Zinc Ion Battery. *Energy Storage Mater.* 38, 590 (2021).
42. J.-G. Wang, H. Liu, R. Zhou, X. Liu, and B. Wei, Onion-like Nanospheres Organized by Carbon Encapsulated Few-Layer MoS_2 Nanosheets with Enhanced Lithium Storage Performance. *J. Power Sourc.* 413, 327 (2019).
43. Z. Zheng, P. Li, J. Huang, H. Liu, Y. Zao, Z. Hu, L. Zhang, H. Chen, M.-S. Wang, D.-L. Peng, and Q. Zhang, High Performance Columnar-like Fe_2O_3 @carbon Composite Anode via yolk@shell Structural Design. *J. Energy Chem.* 41, 126 (2020).
44. D.C. Zuo, S.C. Song, C.S. An, L.B. Tang, Z.J. He, and J.C. Zheng, Synthesis of Sandwich-like Structured Sn/SnO_x @MXene Composite Through in-situ Growth for Highly Reversible Lithium Storage. *Nano Energy* 62, 401 (2019).
45. T. Huang, S. Mao, G. Zhou, Z. Wen, X. Huang, S. Ci, and J. Chen, Hydrothermal Synthesis of Vanadium Nitride and Modulation of its Catalytic Performance for Oxygen Reduction Reaction. *Nanoscale* 6, 9608 (2014).
46. M. Zeiger, T. Ariyanto, B. Krüner, N.J. Peter, S. Fleischmann, B.J.M. Etzold, and V. Presser, Vanadium Pentoxide/Carbide-Derived Carbon Core-Shell Hybrid Particles for High Performance Electrochemical Energy Storage. *J. Mater. Chem. A* 4, 18899 (2016).
47. T. Wang, X. Shen, J. Huang, Q. Xi, Y. Zhao, Q. Guo, X. Wang, and Z. Xu, Tulip-like MoS_2 with a Single Sheet Tapered Structure Anchored on N-Doped Graphene Substrates via C-O-Mo Bonds for Superior Sodium Storage. *J. Mater. Chem. A* 6, 24433 (2018).
48. Y. Li, H. Wen, J. Yang, Y. Zhou, and X. Cheng, Boosting Oxygen Reduction Catalysis with N, F, and S Tri-Doped Porous Graphene: Tertiary N-Precursors Regulates the Constitution of Catalytic Active Sites. *Carbon* 142, 1 (2019).
49. J. Yu, X. Gao, G. Chen, and X. Yuan, Electrocatalytic Performance of Commercial Vanadium Carbide for Oxygen Reduction Reaction. *J. Hydrogen Energy* 41, 4150 (2016).
50. H. Xu, J. Wan, H. Zhang, L. Fang, L. Liu, Z. Huang, J. Li, X. Gu, and Y. Wang, A New Platinum-like Efficient Electrocatalyst for Hydrogen Evolution Reaction at all pH: Single-Crystal Metallic Interweaved V_8C_7 Networks. *Adv. Energy Mater.* 8, 1800575 (2018).
51. J.G. Choi, The Surface Properties of Vanadium Compounds by x-ray Photoelectron Spectroscopy. *Appl. Surf. Sci.* 148, 64 (1999).
52. S. Liao, H. Donggen, D. Yu, Y. Su, and G. Yuan, Preparation and Characterization of ZnO/TiO_2 , $SO_4^{2-}/ZnO/TiO_2$ Photocatalyst and Their Photocatalysis. *J. Photoch. Photobio. A* 168, 7 (2004).
53. L. Shen, H. Lv, S. Chen, P. Kopold, P.A. van Aken, X. Wu, J. Maier, and Y. Yu, Peapod-like Li_3VO_4/N -Doped Carbon Nanowires with Pseudocapacitive Properties as Advanced Materials for High-Energy Lithium-Ion Capacitors. *Adv. Mater.* 29, 1700142 (2017).
54. X. Wang, S. Kajiyama, H. Iinuma, E. Hosono, S. Oro, I. Moriguchi, M. Okubo, and A. Yamada, Pseudocapacitance of MXene Nanosheets for High-Power Sodium-Ion Hybrid Capacitors. *Nat. Commun.* 6, 6544 (2015).
55. F. Niu, N. Wang, J. Yue, L. Chen, J. Yang, and Y. Qian, Hierarchically Porous $CuCo_2O_4$ MicroFlowers: A Superior Anode Material for Li-Ion Batteries and a Stable Cathode Electrocatalyst for $Li-O_2$ Batteries. *Electrochim. Acta* 208, 148 (2016).
56. X. Rui, H. Tan, D. Sim, W. Liu, C. Xu, H.H. Hng, R. Yazami, T.M. Lim, and Q. Yan, Template-Free Synthesis of Urchin-like Co_3O_4 Hollow Spheres with Good Lithium Storage Properties. *J. Power Sources* 222, 97 (2013).

Publisher's Note Springer Nature remains neutral with regard to jurisdictional claims in published maps and institutional affiliations.

Springer Nature or its licensor holds exclusive rights to this article under a publishing agreement with the author(s) or other rightsholder(s); author self-archiving of the accepted manuscript version of this article is solely governed by the terms of such publishing agreement and applicable law.